Chemical Engineering Science 174 (2017) 229–237

Contents lists available at ScienceDirect

Chemical Engineering Science

journal homepage: www.elsevier.com/locate/ces

Analysis of the propylene epoxidation mechanism on supported gold nanoparticles

C. Heath Turner [a,*], Jingjing Ji [a], Zheng Lu [b], Yu Lei [b]

[a] Department of Chemical and Biological Engineering, The University of Alabama, Tuscaloosa, AL 35487, United States
[b] Department of Chemical and Materials Engineering, The University of Alabama in Huntsville, Huntsville, AL 35899, United States

HIGHLIGHTS

- A kinetic Monte Carlo model for direct propylene epoxidation is proposed.
- The kinetic Monte Carlo surface reactions are coupled to a dynamic gas phase.
- Re-adsorption of hydrogen peroxide significantly accelerates the epoxidation.
- Experimental benchmarking tests sensitivity to reactant concentrations.

GRAPHICAL ABSTRACT

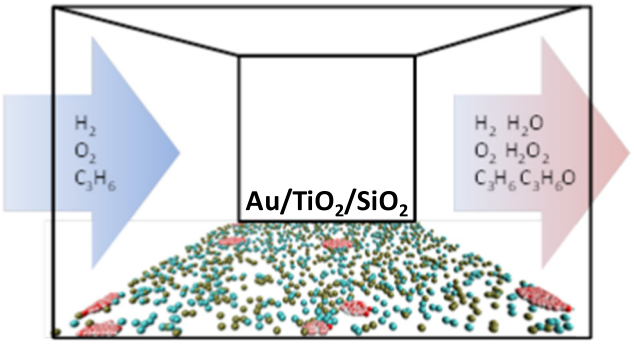

ARTICLE INFO

Article history:
Received 17 June 2017
Received in revised form 8 September 2017
Accepted 9 September 2017
Available online 11 September 2017

Keywords:
Epoxidation
Kinetic Monte Carlo
Gold
Propylene
Simulation
Mechanism

ABSTRACT

The direct propylene epoxidation reaction has been investigated experimentally in the past by several different groups, and gold-based catalysts tend to provide high selectivity for propylene oxide, but the conversion is relatively low. Models that can connect the atomistic catalytic details to the observed experimental data are desired, in order to identify new catalyst structures and formulations. While electronic structure calculations have been used to quantify some of the key reaction steps in the direct propylene epoxidation reaction, atomistic models for translating this information into more experimentally-relevant data are needed. Here, kinetic Monte Carlo (KMC) simulations are used to bridge this gap in the modeling hierarchy. Relevant data from previous experiments and electronic structure calculations are used to parameterize a KMC model for predicting propylene oxide production from an $Au/TiO_2/SiO_2$ catalyst. The model connects the H_2/O_2-related reactions occurring on the Au sites with the epoxidation step on the isolated Ti surface sites. In addition, the composition in the bulk gas phase is synchronized with the dynamic reaction events occurring on the surface. The KMC model is able to adequately reproduce the experimental trends with respect to temperature and different reactant partial pressures. However, this is only achieved by considering the re-adsorption of trace amounts of the oxidant (H_2O_2) from the gas phase, versus merely assuming that desorbed species are immediately swept away in the gas stream.

1. Introduction

Propylene oxide (C_3H_6O, PO) derived from propylene (C_3H_6) is a key chemical intermediate for the production of a number of com-

* Corresponding author.
E-mail address: hturner@eng.ua.edu (C.H. Turner).

http://dx.doi.org/10.1016/j.ces.2017.09.018
0009-2509/

modity chemicals, including polyol, propylene glycol, and glycol ethers (Weissermel, 2003). However, current industrial methods that produce propylene oxide from propylene, namely chlorohydrin and hydroperoxide processes, pose environmental risks because of the production of chlorinated or peroxycarboxylic waste (Monnier, 2001; Nijhuis et al., 2006). Using supported gold-based catalysts to produce propylene oxide directly from propylene and molecular H_2 and O_2 provides an alternative, clean, and potentially more efficient route.

Nearly 20 years ago, Haruta and co-workers discovered that nm-sized Au catalysts on TiO_2 are active and highly selective for the direct gas-phase PO reaction (Hayashi et al., 1998; Uphade et al., 2001; Uphade et al., 2002). When propylene, oxygen, and hydrogen are co-fed, hydrogen peroxide can be readily formed on the surface of gold, and in turn, selectively oxidizes propylene molecules that are adsorbed on TiO_2 sites to propylene oxide (Nijhuis et al., 2006). Also, it has been found that Au supported by titanium silicalite (TS-1) is particularly effective at catalyzing the propylene epoxidation reaction. The isolated Ti active sites are necessary for obtaining a high selectivity towards propylene oxide (Stangland et al., 2000; Nijhuis et al., 1999; Chen et al., 2013a), since propylene oxide molecules that adsorb on adjacent Ti sites lead to catalyst deactivation and the formation of unwanted byproducts. Although the selectivity is very high (>90%), even the best catalysts found to date still suffer from multiple challenges, including low propylene conversion (<10%), poor stability and inefficient usage of H_2 (<50%). Therefore, significant improvement with regard to these issues is necessary, and this requires a more thorough understanding of the underlying chemical reaction network.

A lot of experimental effort has been focused on developing Au-based catalysts for the direct PO reaction (Nijhuis et al., 2006; Chen et al., 2013a, 2013b; Feng et al., 2016; Ferrandez et al., 2015), Also, many related studies have investigated different catalysts for direct H_2O_2 synthesis (Joshi et al., 2007; Landon et al., 2002, 2003; Edwards et al., 2009), since this is a key reaction step prior to the propylene epoxidation. Alternate catalyst formulations have been explored (including Ag, Cu, Mo, as well as photocatalysts) (Ghosh et al., 2014; Lei et al., 2010; Cheng et al., 2014; Chu et al., 2006; Vaughan et al., 2005; Song et al., 2007; Murata et al., 2003; Amano et al., 2004), but performance issues still limit economic viability.

Over the same time period, computational chemistry approaches, mainly first-principles density-functional theory (DFT), have provided additional insights into the chemical mechanisms driving the experimentally-observed PO reaction behavior. These studies have been used to clarify energetic and structural information about the active sites most responsible for the production of PO. For instance, there are DFT reports of the $O_2 + H_2$ reaction mechanisms on Au surfaces and clusters (Wells et al., 2004a; Barton and Podkolzin, 2005), as well as comparisons of the same reactions on other transition metal surfaces (Rh, Ir, Ni, Pd, Pt, Cu, Ag) (Ford et al., 2010; Duzenli et al., 2015) and bimetallic surfaces (Li and Yoshizawa, 2015) (including extrapolations via scaling relations) (Grabow et al., 2012). Computational studies focused exclusively on the direct PO reaction mechanism are more limited, and these have mainly originated from the Thomson (Wells et al., 2004b, 2006; Joshi et al., 2006, 2007) and Corma (Pulido et al., 2012a, 2012b) groups, along with a few related studies of ethylene epoxidation (Karlsen and Schoffel, 1996; Limtrakul et al., 2004). These DFT studies provide an excellent framework for interpreting the experimental results, but due to the variability of experimental sample preparation (structural defects, catalyst particle size distributions, etc.) there can be a wide range of experimentally-observed performance (Qi et al., 2004; Feng et al., 2015a, 2015b; Huang et al., 2010; Lee et al., 2011, 2013, 2014) that is difficult to capture with computationally-expensive DFT approaches. Thus, a lot of the modeling efforts have been more empirical, in order to provide analytical expressions for the product distributions as a function of the natural experimental variables (temperature, reactant partial pressure, feed rates, catalyst loading, etc.). For instance, a series of methodical experimental kinetic tests of the propylene epoxidation performance and related reactions have previously been used to regress reaction orders and elementary reaction steps (Ferrandez et al., 2015; Barton and Podkolzin, 2005; Bravo-Suarez et al., 2008, 2007).

While the DFT-based approaches provide fundamental electronic structure information about ideal systems, and the experimentally-derived rate expressions are useful for optimizing synthesis conditions, there is a large gap between these two ends of the modeling spectrum. More predictive models are needed that can directly connect the atomistic details to the observed experimental behavior. In order to establish this connection, we have pursued a kinetic Monte Carlo (KMC) simulation approach. Fundamental DFT-based values (such as adsorption energies and transition state barriers) can be combined with information about the catalyst surface, in order to make predictions about reactivity on experimentally-relevant time scales. This approach has been pursued previously for modeling heterogeneous catalyst behavior (Hansen and Neurock, 2000; Haug and Raibeck, 2003; Mei et al., 2003, 2006, 2010; Kieken et al., 2005), as well as other activated processes, such as surface deposition (Turner et al., 2016; Jiang and Hou, 2015; Rodgers et al., 2015; Hu et al., 2009a, 2009b; Zheng et al., 2008; Drews et al., 2004; Lou and Christofides, 2004; Wadley et al., 2001), diffusion, (Van der Ven and Ceder, 2000; Greenfield and Theodorou, 2001; Krishnamurthy et al., 2004; Scarle et al., 2005; Munn et al., 2009; Neyertz and Brown, 2010) and electrochemical systems (Lau et al., 2008; Turner et al., 2015).

In the present work, KMC simulations are constructed by selecting a minimal set of systems events relevant to direct PO synthesis (adsorption, desorption, reaction, diffusion), as well as their associated rate expressions. Although the model does not capture all of the possible reactions and side products that are known to exist, it serves as a first step towards developing a stronger connection between the atomistic events and the experimental performance of the direct PO synthesis reaction. This is intended to provide the necessary insight to enable the design of efficient and economical heterogeneous catalysts in the future. In particular, our KMC model is able to adequately reproduce the experimental trends with respect to temperature and different reactant partial pressures. However, we find that this is only achieved by considering the re-adsorption of trace amounts of H_2O_2 from the gas phase, versus merely assuming that the desorbed products are immediately swept away in the gas stream. The next section describes the details of our KMC implementation, followed by our results, experimental benchmarking, and analysis. The conditions for the experimental data used for comparison correspond to a feed gas concentration of 10% H_2, 10% O_2, 10% C_3H_6, and the balance Ar at a total flowrate of 35 ml/min (additional details provided in the Supplementary Information). The coverage of TiO_2 on SiO_2 is approximately 10% and the Au deposition is 1 wt%, and the temperature ranges from 413 to 473 K.

2. Computational methods

The KMC simulation technique originated from the early contributions of Young and Elcock (1966), Cox and Miller (1965)), and Gillespie (1976). In the years following, Fichthorn and Weinberg (1991) provided an additional analysis of the method, and others (Chatterjee and Vlachos, 2007; Voter, 2005) have provided valu-

able critiques and reviews of KMC. In brief, the KMC method can provide an estimate of the time evolution of Markovian processes (Landau and Binder, 2005), as long as there is an accurate set of transition rates characterizing the simulated processes, which are assumed to obey Poisson statistics (Martinez et al., 2008). The KMC simulation approach can typically span time-scales that are orders-of-magnitude beyond traditional molecular dynamics methods, since the KMC simulation time is inversely proportional to the rate of the fastest processes included in the model. This allows systems with activated processes, such as chemical reactions, to be modeled efficiently.

With such a complex catalytic system, involving many steps and surface intermediates, it is unrealistic to expect that our model will fully capture all of the aspects of the experimental system. Thus, along with a well-defined set of experimental benchmark data, we have adopted a minimal event database for modeling the direct PO reaction on TiO_2/SiO_2-supported Au nanoparticles. The experimental catalyst surface ($Au/TiO_2/SiO_2$) is mapped to a 2-D square periodic grid, with a nominal size of 200×200. Smaller grid sizes were also evaluated in preliminary tests (183×183, 141×141, and 115×115), but predicted PO production rates per kg of catalyst varied by no more than 1% with the grid size. Although we are not able to capture the exact crystal structure of the support surface or the Au nanoparticles, the grid spacing is assumed to correspond to a nominal length of 0.288 nm. This resolution allows for a reasonable accounting of the Au catalyst loading, Au size distribution, and occupancy of adsorbates on the surface. According to the experimental loading of Au and TiO_2, the initial SiO_2 surface is decorated with Ti sites, as well as Au nanoparticles of varying diameters. In accordance with the surface grid, the Au nanoparticles were represented as two-dimensional discs on the SiO_2 surface. In the model, the Au nanoparticle diameters were chosen from a random distribution between 2.3 nm and 4.6 nm, while the experimental system corresponds to an average Au particle size of 2.5 nm. The experimental Au loading was approximately 0.1 wt%, and this value was used to make quantitative rate comparisons between the simulations and experiments. Regardless of the exact Au particle sizes in each KMC simulation run, the results are always normalized with respect to the Au mass in each simulation, in order to make consistent comparisons with the experiments. The concentration of Ti sites in the KMC system is set at 10% (experimental surface is estimated at 9.7%), and these are randomly distributed on the surface by direct substitution of the Si sites. A snapshot of the basic model layout is illustrated in Fig. 1.

In order to evaluate the reproducibility of the KMC results, four different independent simulations are performed at each condition, and each simulation is propagated through time for a minimal duration of 500×10^6 KMC steps. These independent simulations allow for statistical fluctuations of the numerical values, but each simulation also corresponds to a slightly different surface configuration (Au particle sizes are chosen from a random distribution mentioned previously, their positions on the SiO_2 surface are randomly assigned, and the Ti site positions also vary). As the simulations proceed, the catalyst structure remains fixed, but the species on the surface can adsorb, desorb, react, and diffuse.

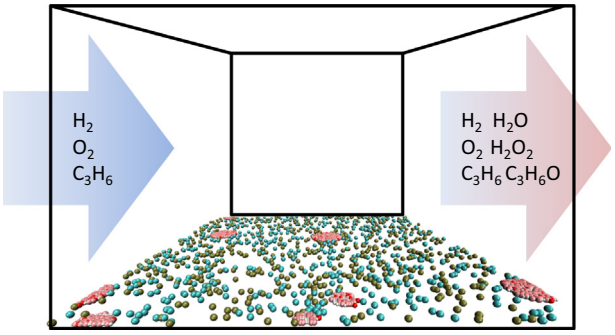

Fig. 1. Illustration of the KMC model system. The two-dimensional periodic catalyst surface is coupled to the gas phase composition via adsorption/desorption steps. On the surface, the red/pink/white sites correspond to different species on the Au nanoparticles, while the cyan/olive sites correspond to different species on the TiO_2/SiO_2 surface.

The system is propagated through time by implementing a KMC algorithm, along with a pre-specified database of system events and rate information. Thus, starting from the initial system configuration on a square lattice, the rate ($\Gamma_{n,site}$) of each event (n) is calculated at each lattice site (x,y), which gives a net event rate of Γ_n, and the total rate of all events in the system is Γ_{total}.

$$\Gamma_n = \sum_x \sum_y \Gamma_{n,site}(x,y) \tag{1}$$

$$\Gamma_{total} = \sum_n \Gamma_n \tag{2}$$

After the system configuration has been defined and the initial rates have been calculated, the system clock is then advanced according to the following equation, where Δt is the time step and RN is a random number, evenly distributed between 0 and 1.

$$\Delta t = -\frac{\ln(RN)}{\Gamma_{total}} \tag{3}$$

After the clock has been incremented, the system configuration is then updated by stochastically choosing an event to occur, according to the probability shown in Eq. (4). Once an event is identified to occur, the system configuration is updated, and the list of event rates is updated (according to the new configuration). At each time step, an event is always performed.

$$P_{n,site} = \frac{\Gamma_{n,site}}{\Gamma_{total}} \tag{4}$$

At the conditions of interest, the selectivity of propylene to propylene oxide conversion is 70–80%. Therefore, at this point, no other side reactions involving propylene are considered in the model. The reacting H_2/O_2 species can form several different intermediates on the Au surface (preferably H_2O_2), but H_2O is also considered, since its formation rate is often competitive with H_2O_2 production. In the experimental system, there is debate about the active oxidant species (H_2O_2 versus —OOH, or possibly both). As a first approximation, we use H_2O_2 as the oxidant. If we also included —OOH as an oxidant, it is unlikely that the results would be significantly different as the surface population of —OOH is typically <10% of the population of H_2O_2 in our model.

A summary of the events that are included in the present systems is provided in Table 1, which includes both forward and reverse events, in order to maintain microscopic reversibility. The rate of reaction, diffusion, and desorption at relevant surface sites is evaluated using Eq. (5) (with $\nu_i = k_B T/h$), while the rate of adsorption on vacant sites is evaluated using Eq. (6).

$$k_i = \nu_i \cdot \exp\left(\frac{-\Delta E_{a,i}}{RT}\right) \tag{5}$$

$$k_{ads,i} = \frac{s_0 \cdot P_i \cdot A_s}{\sqrt{2\pi \cdot MW_i \cdot RT}} \cdot \exp\left(\frac{-\Delta E_{a,i}}{RT}\right) \tag{6}$$

The activation barriers ($\Delta E_{a,i}$) are adapted from previous studies, and the final values used may deviate somewhat from the references provided (e.g., in order to reproduce experimental adsorption behavior or surface coverage in preliminary tests). Also, as a first approximation, neighbor-neighbor interactions are not

Table 1
System events and corresponding activation barriers (in kcal/mol) that are included in the KMC simulations, along with literature references, where applicable. The (*) symbol is used to indicate a surface-bound species.

#	ΔE_a	Event	References
1	0.00	$H_2(g) + (*)Au \rightarrow H_2(*)Au$	–
2	5.50	$H_2(*)Au \rightarrow H_2(g) + (*)Au$	Barton and Podkolzin (2005), Bravo-Suarez et al. (2007) and Barrio et al. (2006)
3	0.00	$O_2(g) + (*)Au \rightarrow O_2(*)Au$	–
4	8.00	$O_2(*)Au \rightarrow O_2(g) + (*)Au$	Bravo-Suarez et al. (2007) and Xu and Mavrikakis (2003)
5	0.00	$C_3H_6(g) + (*)TiO_2 \rightarrow C_3H_6(*)TiO_2$	–
6	16.00	$C_3H_6(*)TiO_2 \rightarrow C_3H_6(g) + (*)TiO_2$	Joshi et al. (2007) and Bravo-Suarez et al. (2007)
7	3.69	$H_2O_2(*)Au \rightarrow H_2O_2(g) + (*)Au$	Wells et al. (2004a, 2004b), Barton and Podkolzin (2005), Ford et al. (2010) and Grabow et al. (2012)
8	3.69	$H_2O_2(*)SiO_2 \rightarrow H_2O_2(g) + (*)SiO_2$	Wells et al. (2004a, 2004b), Barton and Podkolzin (2005), Ford et al. (2010) and Grabow et al. (2012)
9	3.69	$H_2O_2(*)TiO_2 \rightarrow H_2O_2(g) + (*)TiO_2$	Wells et al. (2004a, 2004b), Barton and Podkolzin (2005), Ford et al. (2010) and Grabow et al. (2012)
10	19.72	$C_3H_6(*)TiO_2 + H_2O_2(*)SiO_2 \rightarrow C_3H_6O(*)TiO_2 + H_2O(*)SiO_2$	Wells et al. (2004b) and Joshi et al. (2007)
11	4.00	$C_3H_6O(*)TiO_2 \rightarrow C_3H_6O(g) + (*)TiO_2$	–
12	4.00	$H_2O_2(*)$ diffusion	–
13	6.23	$H_2(*)Au + (*)Au \rightarrow H(*)Au + H(*)Au$	Barton and Podkolzin (2005), Ford et al. (2010), Grabow et al. (2012) and Barrio et al. (2006)
14	6.23	$H(*)Au + H(*)Au \rightarrow H_2(*)Au + (*)Au$	Barton and Podkolzin (2005), Ford et al. (2010), Grabow et al. (2012) and Barrio et al. (2006)
15	47.04	$O_2(*)Au + (*)Au \rightarrow O(*)Au + O(*)Au$	Bravo-Suarez et al. (2007) and Xu and Mavrikakis (2003)
16	17.06	$O(*)Au + O(*)Au \rightarrow O_2(*)Au + (*)Au$	Ford et al. (2010) and Xu and Mavrikakis (2003)
17	2.54	$H_2O(*)Au + O(*)Au \rightarrow OH(*)Au + OH(*)Au$	Ford et al. (2010) and Jiang et al. (2014)
18	0.00	$OH(*)Au + OH(*)Au \rightarrow O(*)Au + H_2O(*)Au$	Ford et al. (2010) and Jiang et al. (2014)
19	2.08	$H_2O(*)Au \rightarrow H_2O(g) + (*)Au$	Barton and Podkolzin (2005), Ford et al. (2010), Jiang et al. (2014) and Huzayyin et al. (2014)
20	10.15	$O(*)Au + H(*)Au \rightarrow OH(*) + (*)Au$	Ford et al. (2010) and Jiang et al. (2014)
21	47.97	$OH(*) + (*)Au \rightarrow O(*)Au + H(*)Au$	Ford et al. (2010) and Jiang et al. (2014)
22	5.76	$H(*)Au + O_2(g) \rightarrow OOH(*)Au$	Wells et al. (2004a) and Ford et al. (2010)
23	13.38	$OOH(*)Au \rightarrow H(*)Au + O_2(g)$	Wells et al. (2004a) and Ford et al. (2010)
24	6.00	$OH(*)Au + H(*)Au \rightarrow H_2O(*)Au + (*)Au$	Ford et al. (2010), Grabow et al. (2012) and Jiang et al. (2014)
25	2.54	$OOH(*)Au + H(*)Au \rightarrow H_2O_2(*)Au + (*)Au$	Ford et al. (2010) and Grabow et al. (2012)
26	7.38	$H_2O_2(*)Au + (*)Au \rightarrow OOH(*)Au + H(*)Au$	Ford et al. (2010) and Grabow et al. (2012)
27	11.76	$H_2O_2(*)Au + (*)Au \rightarrow OH(*)Au + OH(*)Au$	Ford et al. (2010) and Grabow et al. (2012)
28	11.76	$OOH(*)Au + (*)Au \rightarrow OH(*)Au + O(*)Au$	Grabow et al. (2012)
29	16.60	$OH(*)Au + O(*)Au \rightarrow OOH(*)Au + (*)Au$	Ford et al. (2010)
30	33.21	$OH(*)Au + OH(*)Au \rightarrow H_2O_2(*)Au + (*)Au$	Barton and Podkolzin (2005) and Ford et al. (2010)
31	3.69	$OOH(*)Au + H(*)Au \rightarrow OOHH(*)Au + (*)Au$	Ford et al. (2010)
32	5.76	$OOHH(*)Au + (*)Au \rightarrow OOH(*)Au + H(*)Au$	Ford et al. (2010)
33	1.61	$OOHH(*)Au \rightarrow O(*)Au + H_2O(g)$	Ford et al. (2010)
34	44.51	$O(*)Au + H_2O(g) \rightarrow OOHH(*)Au$	Ford et al. (2010)
35	0.00	$H_2O_2(g) + (*)Au \rightarrow H_2O_2(*)Au$	–
36	0.00	$H_2O_2(g) + (*)Si \rightarrow H_2O_2(*)Si$	–
37	0.00	$H_2O_2(g) + (*)Ti \rightarrow H_2O_2(*)Ti$	–
38	0.00	$H_2O(g) + (*)Au \rightarrow H_2O(*)Au$	–
39	43.12	$H_2O(*)Au + (*)Au \rightarrow OH(*)Au + H(*)Au$	Ford et al. (2010)
40	4.00	$H_2O(*)$ diffusion	–
41	12.00	$H_2(*)$ diffusion	Santiago-Rodriguez et al. (2014)
42	12.88	$O_2(*)$ diffusion	Santiago-Rodriguez et al. (2014)
43	3.46	$H(*)$ diffusion	Santiago-Rodriguez et al. (2014)
44	12.91	$O(*)$ diffusion	Santiago-Rodriguez et al. (2014)
45	2.31	$OH(*)$ diffusion	Santiago-Rodriguez et al. (2014)

assumed to affect the rates of the individual events, and the default sticking coefficients (s_0) are given a value of 1.0. In these equations, h is Plank's constant, k_B is Boltzmann's constant, P_i is the partial pressure of species i, R is the gas constant, MW_i is the molecular weight of species i, and A_s is the area of the adsorption site (corresponding to the area of an individual grid cell).

It should be noted that the kinetic constants used in our model are unlikely to be unique to our results. Due to possible cancellation of errors, each of the kinetic constants in Table 1 could vary slightly, but still yield indistinguishable results. In order to probe such behavior, which is common to multi-parameter models, a comprehensive sensitivity analysis should be performed, which we intend to explore in future work. Others have recently reported rigorous and efficient approaches for performing quantitative error analysis of KMC simulations (Hoffmann et al., 2017).

There are several practical hurdles that challenge our implementation of KMC to the direct PO reaction. First, due to the variety of events and reactions that are included in our database of system events, there is an extremely wide range of event probabilities that must be captured. For instance, fast events (like diffusion, with low activation barriers) will statistically dominate the moves performed in the simulation, while slow events (like chemical reactions, with high activation barriers) may have rates so low that they are not sampled during a typical simulation. In our case, the last step in the reaction mechanism, the epoxidation of propylene on the Ti sites, has a relatively high activation barrier, yet it is a critical reaction that must be adequately sampled. Second, our reaction system is somewhat more complicated than that encountered in other KMC studies. For instance, instead of following a single reaction zone (or simple surface deposition), we consider the H_2/O_2-related reactions on the Au nanoparticles, followed by transport of the oxidant to the Ti sites, which are then responsible for the epoxidation of adsorbed propylene. Coupling the events that are occurring at the different reaction zones (as well as the oxidant transport) also leads to challenges of sampling efficiency. This reaction/diffusion co-dependency also hampers the direct numerical modeling of this system by solving a set of chemical rate equations (i.e., motivating our KMC-based approach). Third, as is

common to many KMC studies, our rate database contains a heterogeneous mix of both rigorous and estimated values. Some of the events and rates have been thoroughly studied, but many of the reaction/adsorption/diffusion events have not received adequate attention (or their reported rates vary by many orders-of-magnitude). While we are not able to completely address this information gap, our experimental benchmarking provides some confidence in our event database. In addition, our KMC model can provide some insight into the relative sensitivity of the model predictions to the individual event rates, in order to highlight the steps that deserve the most scrutiny in the future.

In order to deal with the inherent time-scale challenges mentioned above (due to the wide range of reaction rates and necessary diffusion events), others have proposed some possible solutions. For instance, Samant and Vlachos (2005) developed a multiscale KMC technique to deal with such systems. In their approach, the underlying KMC engine alternates between periods of sampling the fast events and periods of sampling the slow events (within the limit of well-equilibrated fast events). The extent of equilibration of the slow events is evaluated on-the-fly by quantifying the deviation in the quasi-equilibrated populations. Other accelerated KMC techniques have been reported, such as the τ-leap method (Gillespie, 2001; Vlachos, 2008), and an overview of many similar techniques were reviewed a decade ago by Chatterjee and Vlachos (2007).

We have pursued a slightly different technique for enhancing the sampling efficiency, but it reflects some of the same basic concepts as mentioned in the examples above. In our simulations, a critical event is the oxidation of propylene at the Ti site. However, this reaction has a high barrier (relative to the other system events), and the sampling is compounded by the fact that it is rare for the oxidizing species (H_2O_2) to be in close proximity to this site, due to the short lifetime and low concentration of the H_2O_2 species. As a result, we artificially reduced the activation barrier for the propylene epoxidation step, in order to improve sampling, and then used a simple scaling relationship to extrapolate the simulation results to correspond to the full activation barrier value. This is similar to the accelerated sampling approach very recently introduced by Neurock and coworkers (Dybeck et al., 2017). Tests were performed to check for any unintended deviations in other quantities (surface coverages of individual species, adsorption/desorption rates, etc.).

A unique aspect of our KMC simulations is the coupling between the surface adsorption/desorption events and the bulk gas phase composition. This allowed for the product species to potentially re-adsorb onto the surface. Even though the variations in the gas phase composition were very small, there were measurable changes in the overall production rates of H_2O_2, H_2O, and PO, when this coupling between the gas phase and the surface was permitted. In most past KMC models of surface catalysis (Hansen and Neurock, 2000; Lorenzi et al., 2016; Reuter, 2016; Saeys et al., 2005), the gas concentration is held fixed, and it is assumed that the reaction products from the surface are swept away as soon as they are desorbed (preventing re-adsorption and further reaction). In general, this is a reasonable assumption with minimal impact on the predicted catalytic properties. However, in our system, the trace amounts of H_2O_2 are important to quantify, since its concentration can significantly impact the simulation results. Thus, in our simulations, there is a small volume element above the surface which represents the bulk gas phase, with horizontal (x,y) dimensions identical to the catalyst surface and a vertical (z) dimension equal to five times the length of the (x,y) dimension. Within this bulk volume (1.15×10^7 nm^3), the concentration is updated at each KMC step by accounting for the flux of fresh feed gas (of a pre-specified inlet composition), as well as any adsorption/desorption steps occurring on the surface.

The appropriate volume of the bulk gas phase above the surface, as well as the exact value of the incoming flux of fresh feed gas within this volume element, cannot be rigorously benchmarked against the experiments. However, the intent was to capture the possibility of re-adsorption of small amounts of product species back onto the surface from an effective boundary layer. We set the feed gas flux equivalent to a nominal residence time value of 1.42×10^{-5} s. While this is a small value, it reflects the limited size of our model (length-scale on the order of nanometers). This is orders-of-magnitude smaller than the experimental systems, so we normalize our simulated results on a mass-weighted basis in order to facilitate comparisons with the experiments. At the conditions explored, this yielded typical gas-phase concentrations of H_2 = 9.87%, O_2 = 9.95%, C_3H_6 = 10.02%, H_2O_2 < 0.01%, H_2O = 0.14%, and C_3H_6O < 0.01%, but of course, these values vary slightly at different operating conditions. In order to test the sensitivity of our results to the details of the gas flux, a sensitivity analysis is performed.

Although rare, there have been other attempts at connecting KMC simulations with a dynamic gas phase composition. For instance, Reuter and coworkers (Matera et al., 2014) recently introduced a protocol for coupling a computational fluid dynamics (CFD) transport model with a KMC reaction model. The CFD model provided information about the local gas-phase concentrations above the catalyst surface, while a set of KMC simulations involving a set of chemical reactions were performed at discrete locations on the surface (each corresponding to the local gas-phase concentrations). This approach can provide some important insight into this atomistic-level reaction-diffusion behavior. In our work, we treat the gas phase with less detail, but our surface model preserves the catalyst structure, which is critical to the propylene epoxidation reaction being presently modeled.

3. Results and discussion

The main H_2/O_2 reactions and rates were adapted from the DFT calculations of Ford et al. (2010), and these reactions account for the H_2O_2 and H_2O formation on an Au(1 1 1) surface. Although nm-sized Au clusters are expected to have many edge sites, leading to different activation barriers for the reactions, other computational studies have predicted that Au(1 1 1) terrace sites and Au (2 1 1) steps have almost identical H_2O_2 formation rates and selectivity (Grabow et al., 2012). The epoxidation step is assumed to involve the direct reaction between H_2O_2 and C_3H_6 molecules adsorbed on Ti sites. The Thomson group has calculated the barrier for this reaction to be 19.9 kcal/mol within TS-1 catalyst pores (Joshi et al., 2007), but the local structure can alter this value to as low as 9.3 kcal/mol near surface defects (Wells et al., 2004b). Experimental studies of the direct PO reaction on Au/TS-1 and Au-Ti-TUD catalysts have been used to empirically estimate a PO rate barrier of 8.4–13.1 kcal/mol (Taylor et al., 2006; Lu et al., 2007). The experimental samples in our current work have been prepared with atomic-layer deposition (see additional details in Supporting Information) and are likely to be best represented by the ideal TS-1 model used in the previous DFT calculations, corresponding to a PO activation barrier of 19.9 kcal/mol.

In our KMC model, we have estimated our ΔE_a value to be closer to the most recent DFT result. As mentioned previously, this high ΔE_a value creates a statistical sampling challenge, so we have artificially lowered the PO formation barrier (over a range of 12–15 kcal/mol). Using this range of artificially-low values, the overall PO formation rates predicted from the KMC simulations follow an Arrhenius relationship (Fig. 2), so that the behavior at higher E_a values can be easily extrapolated. The statistic error of the KMC-predicted PO formation rates reported throughout our work ranges

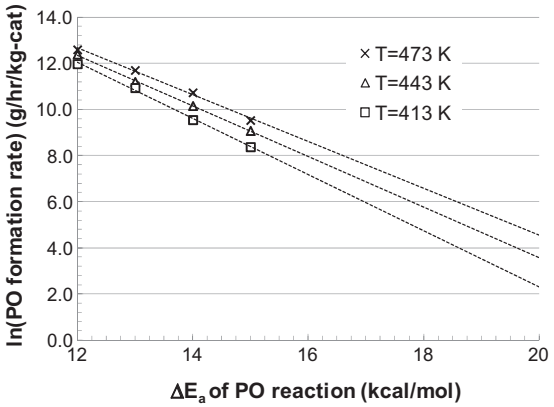

Fig. 2. Scaling behavior of the overall PO formation rate predicted from the KMC simulations, with respect to changes in the activation barrier of the reaction between hydrogen peroxide and propylene.

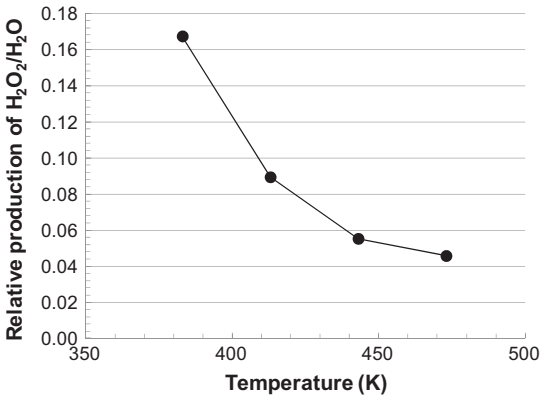

Fig. 4. Relative production of H_2O_2 versus H_2O, as a function of the temperature predicted from KMC simulations. The standard deviation of the data gradually increases from approximately 1% at 383 K–10% at 473 K.

from 5 to 8%, based on the results from four different independent simulations, with explicit error bars included in the experimental comparison shown in Fig. 3. The correlation coefficient for the three fitted trend lines in Fig. 2 are over 0.998, and the slopes of the trend lines gradually decrease with respect to temperature: −1.22, −1.10, and −1.02 at 413 K, 443 K, and 473 K, respectively. When the KMC data are extrapolated to the higher ΔE_a values, the results can be closely aligned with the experimental results. For instance, with an ΔE_a value of 19.72 kcal/mol (very similar to the previous DFT calculation), the KMC results fall within reasonable agreement of the experimental data, as shown in Fig. 3.

Although the PO selectivity can be very high with Au-based catalysts, the efficient formation of hydrogen peroxide can be a major issue of concern, since it can limit the PO formation rate. The H_2O_2 species is unstable, and formation of PO requires that the H_2O_2 molecules diffuse to the edge of the gold nanoparticle or transport to some other location on the surface to react with propylene (where Ti sites exist). The KMC simulations predict that the ratio of H_2O_2:H_2O present in the exit gas stream ranges from 17% down to 4%, as the temperature increases from 383 K to 473 K (Fig. 4). Experimentally, 30% H_2 efficiency has been previously obtained (Huang and Haruta, 2012), but the benchmark for achieving industrial economic viability is closer to 50% (Sinha et al., 2004). Thus, as the temperature increases, the PO reaction rate will naturally increase, but its formation is also balanced by the availability of H_2O_2, since the H_2O_2 is more quickly converted to H_2O at the higher temperatures.

With our KMC simulations, we can make several comparisons directly against the experimental data to benchmark our underlying model development. For instance, we can test different feed compositions, flow rates, and temperatures and predict the results on the PO formation rate, surface coverage, product distribution, etc.

The PO formation rate is found to only be mildly sensitive to the partial pressure of O_2 gas in the feed stream. In the experiments, this aspect is probed at a fixed temperature of 453 K, with both the H_2 and C_3H_6 gas phase mole fractions set at 10%. In order to analyze the results, we have compared the PO formation rate with different O_2 feed gas compositions, relative to the base case when all three entering gas species are set at 10%. Overall, the results shown in Fig. 5 are very consistent, indicating that there is a moderate positive correlation between the change in the O_2 concentration and the PO formation rate, and the KMC model does a good job of capturing this behavior. It was initially expected that this positive trend would be reflected in an increase in the relative H_2O_2/H_2O production rate. However, this ratio actually decreases slightly. As the O_2 feed concentration increases from 4% to 12%, the relative H_2O_2/H_2O production rate decreases from a value of 0.595 to a value of 0.544. The moderately increased PO production rate illustrated in Fig. 5 seems to be related to the fact that although the *relative* H_2O_2 production rate decreases (versus H_2O), the total concentration of H_2O_2 in the gas phase actually

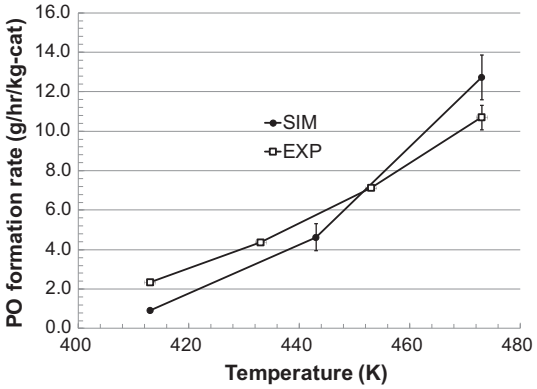

Fig. 3. Comparison of experimental and extrapolated KMC simulation of the PO formation rate, achieved using an ΔE_a value of 19.72 kcal/mol for the PO reaction step. The error bars indicate the standard deviation, which is smaller than the symbol in some cases.

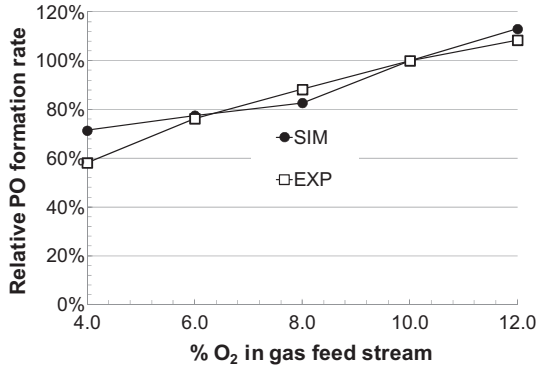

Fig. 5. Comparison of the relative shifts in the PO formation rate from both simulations and experiments, as a function of the O_2 concentration in the gas feed stream. The temperature is 453 K, and the concentrations of H_2 and C_3H_6 in the feed gas are both set at 10%.

Table 2
Relative PO production rate at different gas feed compositions, compared to the default concentration of 10% for all gases, as well as the corresponding H_2O_2 composition in the gas phase. The temperature corresponds to 413 K, and the concentration of O_2 gas in the feed is held fixed at 10%. Standard deviations are indicated in parentheses.

Gas feed composition		Relative PO production rate		H_2O_2% (g)
H_2%	C_3H_6%	Experiment (%)	Simulation (%)	Simulation
6.0	14.0	77(1)	47(8)	0.0058(4)
14.0	6.0	110(10)	155(9)	0.0131(5)
6.0	10.0	–	48(7)	0.0056(2)
8.0	10.0	–	84(10)	0.0069(5)
12.0	10.0	–	106(6)	0.0123(4)
14.0	10.0	–	143(14)	0.0145(11)

increases by over 20% over this same range. Thus, despite the selectivity of H_2O to H_2O_2 production, the increased availability of H_2O_2 in the gas phase is likely responsible for accelerating the PO formation.

Additional comparisons have been made by varying the concentrations of the other reactant gases in the feed stream. The mole fractions of the H_2 and C_3H_6 species in the feed were varied from the default values of 10% each, to values of 6% H_2/14% C_3H_6 and 14% H_2/6% C_3H_6. When the KMC results are benchmarked against the experimental values, the trends in the PO production rate are captured, but there is not quantitative agreement (see Table 2). As before, there seems to be a strong positive correlation with the H_2O_2 concentration in the gas phase. When the total H_2 gas feed concentration increases (decreases) by 4%, equivalent to a relative change of ±40%, the H_2O_2 concentration in the gas phase increases (decreases) by approximately 84% (20%), and this is likely responsible for the large change in the PO formation rate. The experimental data indicate a PO reaction order of ~0.2 with respect to the H_2 concentration, while the KMC simulations predict a result of >1.0 and previous experimental results from similar systems indicate a reaction order of 0.40–0.50 (Hayashi et al., 1998; Stangland et al., 2000).

The sensitivity of the KMC simulations to the H_2/C_3H_6 feed composition highlights an opportunity for future model improvement. For instance, adding additional reaction channels (i.e., production of ethanal, propane, acetone, etc.) may create alternate sinks for the H_2, mitigating its direct sensitivity on the production of PO. This modification would be consistent with the experimentally-observed reaction orders of these side-products with respect to the H_2 concentration (Stangland et al., 2000). Also, the adsorption/desorption rate expressions for the H_2 molecules deserve further scrutiny, since the surface coverage of H and related hydrogenation reactions will be affected by the overall hydrogen balance in the system.

One of the more surprising outcomes from the KMC simulations is that the production of PO seems to depend strongly on the re-adsorption of the H_2O_2 (and hence, the gas phase concentration). Once H_2O_2 is formed on the Au sites, it can ultimately either desorb (with a low activation barrier), it can degrade to H_2O (with a low activation barrier), or it can diffuse to a Ti site and potentially react with an adsorbed C_3H_6 molecule. Due to these alternate pathways, the probability of an H_2O_2 molecule surviving on the surface and successfully diffusing to a C_3H_6-occupied Ti site is extremely rare, leading to almost zero PO production over the course of a typical simulation. However, when re-adsorption from the gas phase is enabled, the probability of an encounter between the C_3H_6 and the H_2O_2 is significantly increased (even though the gas-phase concentration of H_2O_2 is $\ll$1%).

Due to this apparent connection between the gas phase product concentrations and the surface reactions, a closer analysis of the gas phase details was performed. While the gas phase product concentrations are very low, they can be further diluted by increasing the flux of the incoming feed gas, and this decreases their re-adsorption rate onto the catalyst surface. A sensitivity analysis was performed by varying the gas phase residence time over a range of five orders of magnitude and calculating the change in the PO production rate, as shown in Fig. 6.

The predicted PO formation rate as a function of the feed gas residence time displays a volcano-like trend, and this can be correlated to changes in the gas-phase concentration of H_2O_2. For instance, Fig. 7 shows the gas phase composition of H_2O and H_2O_2 as a function of the residence time, and although the H_2O shows a monotonic increase as a function of the residence time, the H_2O_2 concentration is maximized at a residence time of approximately 10^{-4} s, similar the PO formation rate shown in Fig. 6. The shape of the H_2O_2 concentration data in Fig. 7 arises from a competition between two different mechanisms. First, as

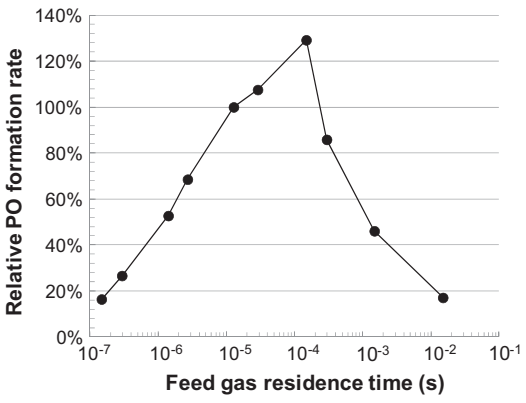

Fig. 6. Relative change in the PO production rate as a function of the feed gas residence time (reference value of 1.42×10^{-5} s) at a temperature of 473 K.

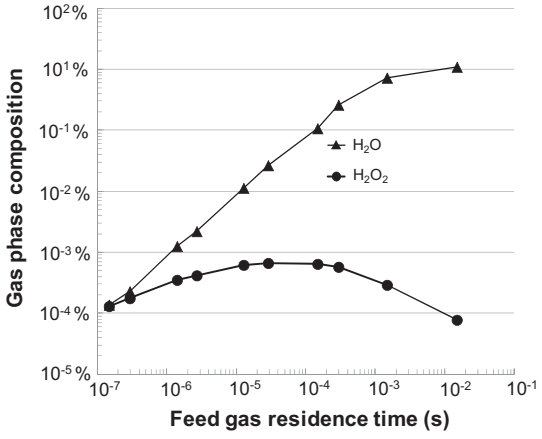

Fig. 7. Gas phase composition of H_2O and H_2O_2 as a function of the feed gas residence time at a temperature of 473 K.

the residence time is initially increased, the longer residence time allows for a gradual accumulation of H_2O_2 in the system. However, as the residence time continues to increase, the conversion of H_2O_2 to H_2O begins to dominate in the system, leading to a decline of H_2O_2 (and a corresponding decrease of the PO formation rate). Thus, regardless of the activity of the catalyst, the actual availability of the H_2O_2 is a key factor in maximizing the synthesis of PO. This trend is also reflected in Table 2, which includes data for the corresponding H_2O_2 composition in the gas phase.

4. Conclusions

In this work, KMC simulations are used to model the direct epoxidation of propylene to propylene oxide on an $Au/TiO_2/SiO_2$ catalyst. Although the model is a simple two-dimensional representation of the actual catalyst surface, the basic catalyst features are preserved (Ti concentration, Au loading, Au particle sizes), and the KMC results are benchmarked against relevant experimental data. In addition, the composition in the bulk gas phase is synchronized with the dynamic reaction events occurring on the surface, and this coupling allows us to relax the typical assumption of a constant gas-phase composition. By acquiring mechanistic information from various DFT studies, and compiling this information into a KMC model, several aspects of the experimental catalytic behavior can be captured. In particular, we can model the reaction and surface transport processes simultaneously in the KMC simulations (i.e., proximity of reactants to the active sites), and this is difficult to replicate with other modeling techniques. We find close agreement between the KMC simulations and the experimental data in several aspects, but this is only achieved by considering the re-adsorption of trace amounts of the oxidant (H_2O_2) from the gas phase.

An obvious shortcoming in the KMC model is the H_2 sensitivity, which is higher than in most previous experimental studies. This may be an artifact that arises from our neglect of other competing reaction channels on the catalyst surface which may serve as hydrogen sinks. Also, several of the individual event rates used in the model deserve additional scrutiny. If some of these secondary effects can be resolved, this approach can provide an excellent modeling tool for connecting the atomistic-level features of such a catalytic system to the predicted experimental behavior. In particular, bimetallic catalyst and optimally-designed supports will likely be needed for advancing the direct synthesis of propylene oxide beyond current limits, while maximizing the availability of the oxidizing species near the Ti sites is critical for accelerating the production of PO.

Acknowledgements

Financial support for this work was provided by the National Science Foundation (CBET-151048 and CBET-1511820) and a UA System Collaboration Grant.

Appendix A. Supplementary material

Supplementary data associated with this article can be found, in the online version, at http://dx.doi.org/10.1016/j.ces.2017.09.018.

References

Amano, F., Tanaka, T., Funabiki, T., 2004. Langmuir 20 (10), 4236–4240.
Barrio, L., Liu, P., Rodriguez, J.A., Campos-Martin, J.M., Fierro, J.L.G., 2006. J. Chem. Phys. 125 (16), 164715.
Barton, D.G., Podkolzin, S.G., 2005. J. Phys. Chem. B 109 (6), 2262–2274.
Bravo-Suarez, J.J., Lu, J., Dallos, C.G., Fujitani, T., Oyama, S.T., 2007. J. Phys. Chem. C 111 (46), 17427–17436.
Bravo-Suarez, J.J., Bando, K.K., Lu, J., Haruta, M., Fujitani, T., Oyama, S.T., 2008. J. Phys. Chem. C 112 (4), 1115–1123.
Chatterjee, A., Vlachos, D.G., 2007. J. Comput. Aided Mater. Des. 14 (2), 253–308.
Chen, J., Halin, S.J.A., Pidko, E.A., Verhoeven, M.W.G.M., Perez Ferrandez, D.M., Hensen, E.J.M., Schouten, J.C., Nijhuis, T.A., 2013a. ChemCatChem 5 (2), 467–478.
Chen, J.Q., Pidko, E.A., Ordomsky, V.V., Verhoeven, T., Hensen, E.J.M., Schouten, J.C., Nijhuis, T.A., 2013b. Catal. Sci. Technol. 3 (11), 3042–3055.
Cheng, L., Yin, C., Mehmood, F., Liu, B., Greeley, J., Lee, S., Lee, B., Seifert, S., Winans, R. E., Teschner, D., Schloegl, R., Vajda, S., Curtiss, L.A., 2014. ACS Catal. 4 (1), 32–39.
Chu, H., Yang, L., Zhang, Q.H., Wang, Y., 2006. J. Catal. 241 (1), 225–228.
Cox, D.R., Miller, H.D., 1965. The Theory of Stochastic Processes. Methuen, London.
Drews, T.O., Braatz, R.D., Alkire, R.C., 2004. Int. J. Multiscale Comput. Eng. 2 (2), 313–327.
Duzenli, D., Atmaca, D.O., Gezer, M.G., Onal, I., 2015. Appl. Surf. Sci. 355, 660–666.
Dybeck, E.C., Plaisance, C.P., Neurock, M., 2017. J. Chem. Theory Comput. 13 (4), 1525–1538.
Edwards, J. K., Solsona, B., Ntainjua, E.N., Carley, A.F., Herzing, A.A., Kiely, C.J., Hutchings, G.J., Science 2009, 323(5917), 1037–1041.
Feng, X., Duan, X.Z., Cheng, H.Y., Qian, G., Chen, D., Yuan, W.K., Zhou, X.G., 2015a. J. Catal. 325, 128–135.
Feng, X., Duan, X.Z., Yang, J., Qian, G., Zhou, X.G., Chen, D., Yuan, W.K., 2015b. Chem. Eng. J. 278, 234–239.
Feng, X., Liu, Y.B., Li, Y.C., Yang, C.H., Zhang, Z.H., Duan, X.Z., Zhou, X.G., Chen, D., 2016. AIChE J. 62 (11), 3963–3972.
Ferrandez, D.M.P., Fernandez, I.H., Teley, M.P.G., de Croon, M., Schouten, J.C., Nijhuis, T.A., 2015. J. Catal. 330, 396–405.
Fichthorn, K.A., Weinberg, W.H., 1991. J. Chem. Phys. 95 (2), 1090–1096.
Ford, D.C., Nilekar, A.U., Xu, Y., Mavrikakis, M., 2010. Surf. Sci. 604 (19–20), 1565–1575.
Ghosh, S., Acharyya, S.S., Tiwari, R., Sarkar, B., Singha, R.K., Pendem, C., Sasaki, T., Bal, R., 2014. ACS Catal. 4 (7), 2169–2174.
Gillespie, D.T., 1976. J. Comput. Phys. 22 (4), 403–434.
Gillespie, D.T., 2001. J. Chem. Phys. 115 (4), 1716–1733.
Grabow, L.C., Hvolbaek, B., Falsig, H., Norskov, J.K., 2012. Top. Catal. 55 (5–6), 336–344.
Greenfield, M.L., Theodorou, D.N., 2001. Macromolecules 34 (24), 8541–8553.
Hansen, E.W., Neurock, M., 2000. J. Catal. 196 (2), 241–252.
Haug, K., Raibeck, G., 2003. J. Phys. Chem. B 107 (41), 11433–11440.
Hayashi, T., Tanaka, K., Haruta, M., 1998. J. Catal. 178 (2), 566–575.
Hoffmann, M.J., Engelmann, F., Matera, S., 2017. J. Chem. Phys. 146 (4), 044118.
Hu, G., Orkoulas, G., Christofides, P.D., 2009a. Chem. Eng. Sci. 64 (17), 3903–3913.
Hu, G., Orkoulas, G., Christofides, P.D., 2009b. Ind. Eng. Chem. Res. 48 (14), 6690–6700.
Huang, J.H., Haruta, M., 2012. Res. Chem. Intermed. 38 (1), 1–24.
Huang, J.H., Takei, T., Akita, T., Ohashi, H., Haruta, M., 2010. Appl. Catal. B-Environ. 95 (3–4), 430–438.
Huzayyin, A., Chang, J.H., Lian, K., Dawson, F., 2014. J. Phys. Chem. C 118 (7), 3459–3470.
Jiang, H., Hou, Z., 2015. J. Chem. Phys. 143 (8), 084109.
Jiang, Z., Li, M.M., Yan, T., Fang, T., 2014. Appl. Surf. Sci. 315, 16–21.
Joshi, A.M., Delgass, W.N., Thomson, K.T., 2006. J. Phys. Chem. B 110 (6), 2572–2581.
Joshi, A.M., Delgass, W.N., Thomson, K.T., 2007. J. Phys. Chem. C 111 (20), 7384–7395.
Joshi, A.M., Delgass, W.N., Thomson, K.T., 2007. J. Phys. Chem. C 111 (22), 7841–7844.
Karlsen, E., Schoffel, K., 1996. Catal. Today 32 (1–4), 107–114.
Kieken, L.D., Neurock, M., Mei, D.H., 2005. J. Phys. Chem. B 109 (6), 2234–2244.
Krishnamurthy, R., Yoon, Y.G., Srolovitz, D.J., Car, R., 2004. J. Am. Ceram. Soc. 87 (10), 1821–1830.
Landau, D.P., Binder, K., 2005. A Guide to Monte Carlo Simulations in Statistical Physics. United Kingdom, Cambridge.
Landon, P., Collier, P.J., Papworth, A.J., Kiely, C.J., Hutchings, G.J., 2002. Chem. Commun. (18), 2058–2059
Landon, P., Collier, P.J., Carley, A.F., Chadwick, D., Papworth, A.J., Burrows, A., Kiely, C.J., Hutchings, G.J., 2003. Phys. Chem. Chem. Phys. 5 (9), 1917–1923.
Lau, K.C., Turner, C.H., Dunlap, B.I., 2008. Solid State Ionics 179 (33–34), 1912–1920.
Lee, W.-S., Zhang, R., Akatay, M.C., Baertsch, C.D., Stach, E.A., Ribeiro, F.H., Delgass, W.N., 2011. ACS Catal. 1 (10), 1327–1330.
Lee, W.-S., Akatay, M.C., Stach, E.A., Ribeiro, F.H., Delgass, W.N., 2013. J. Catal. 308, 98–113.
Lee, W.S., Akatay, M.C., Stach, E.A., Ribeiro, F.H., Delgass, W.N., 2014. J. Catal. 313, 104–112.
Lei, Y., Mehmood, F., Lee, S., Greeley, J., Lee, B., Seifert, S., Winans, R.E., Elam, J.W., Meyer, R.J., Redfern, P.C., Teschner, D., Schlogl, R., Pellin, M.J., Curtiss, L.A., Vajda, S., 2010. Science 328 (5975), 224–228.
Li, J., Yoshizawa, K., 2015. Catal. Today 248, 142–148.
Limtrakul, J., Inntam, C., Truong, T.N., 2004. J. Mol. Catal. A-Chem. 207 (2), 139–148.
Lorenzi, J.M., Matera, S., Reuter, K., 2016. ACS Catal. 6 (8), 5191–5197.
Lou, Y.M., Christofides, P.D., 2004. Comput. Chem. Eng. 29 (1), 225–241.
Lu, J.Q., Zhang, X.M., Bravo-Suarez, J.J., Tsubota, S., Gaudet, J., Oyama, S.T., 2007. Catal. Today 123 (1–4), 189–197.
Martinez, E., Marian, J., Kalos, M.H., Perlado, J.M., 2008. J. Comput. Phys. 227 (8), 3804–3823.
Matera, S., Maestri, M., Cuoci, A., Reuter, K., 2014. ACS Catal. 4 (11), 4081–4092.
Mei, D.H., Hansen, E.W., Neurock, M., 2003. J. Phys. Chem. B 107 (3), 798–810.

Mei, D., Sheth, P.A., Neurock, M., Smith, C.M., 2006. J. Catal. 242 (1), 1–15.
Mei, D., Du, J., Neurock, M., 2010. Ind. Eng. Chem. Res. 49 (21), 10364–10373.
Monnier, J.R., 2001. Appl. Catal. A-General 221 (1–2), 73–91.
Munn, R.W., Eilmes, A., Scarle, S., Sterzel, M., 2009. Mater. Sci.-Poland 27 (3), 637–647.
Murata, C., Yoshida, H., Kumagai, J., Hattori, T., 2003. J. Phys. Chem. B 107 (18), 4364–4373.
Neyertz, S., Brown, D., 2010. Macromolecules 43 (21), 9210–9214.
Nijhuis, T.A., Huizinga, B.J., Makkee, M., Moulijn, J.A., 1999. Ind. Eng. Chem. Res. 38 (3), 884–891.
Nijhuis, T.A., Makkee, M., Moulijn, J.A., Weckhuysen, B.M., 2006. Ind. Eng. Chem. Res. 45 (10), 3447–3459.
Pulido, A., Boronat, M., Corma, A., 2012a. J. Phys. Chem. C 116 (36), 19355–19362.
Pulido, A., Concepcion, P., Boronat, M., Corma, A., 2012b. J. Catal. 292, 138–147.
Qi, C., Okumura, M., Akita, T., Haruta, M., 2004. Appl. Catal. A-General 263 (1), 19–26.
Reuter, K., 2016. Catal. Lett. 146 (3), 541–563.
Rodgers, W.J., May, P.W., Allan, N.L., Harvey, J.N., 2015. J. Chem. Phys. 142 (21), 214707.
Saeys, M., Reyniers, M.F., Thybaut, J.W., Neurock, M., Marin, G.B., 2005. J. Catal. 236 (1), 129–138.
Samant, A., Vlachos, D.G., 2005. J. Chem. Phys. 123 (14), 144114.
Santiago-Rodriguez, Y., Herron, J.A., Curet-Arana, M.C., Mavrikakis, M., 2014. Surf. Sci. 627, 57–69.
Scarle, S., Sterzel, M., Eilmes, A., Munn, R.W., 2005. J. Chem. Phys. 123 (15), 154909.
Sinha, A.K., Seelan, S., Tsubota, S., Haruta, M., 2004. Angewandte Chemie-International Edition 43 (12), 1546–1548.
Song, Z.X., Mimura, N., Bravo-Suarez, J.J., Akita, T., Tsubota, S., Oyama, S.T., 2007. Appl. Catal. A-General 316 (2), 142–151.
Stangland, E.E., Stavens, K.B., Andres, R.P., Delgass, W.N., 2000. J. Catal. 191 (2), 332–347.
Taylor, B., Lauterbach, J., Blau, G.E., Delgass, W.N., 2006. J. Catal. 242 (1), 142–152.
Turner, C.H., Zhang, Z.T., Gelb, L.D., Dunlap, B.I., 2015. Rev. Comput. Chem. 28 (28), 175–204.
Turner, C.H., Lei, Y., Bao, Y.P., 2016. Nanoscale 8 (17), 9354–9365.
Uphade, B.S., Yamada, Y., Akita, T., Nakamura, T., Haruta, M., 2001. Appl. Catal. A-General 215 (1–2), 137–148.
Uphade, B.S., Akita, T., Nakamura, T., Haruta, M., 2002. J. Catal. 209 (2), 331–340.
Van der Ven, A., Ceder, G., 2000. Electrochem. Solid State Lett. 3 (7), 301–304.
Vaughan, O.P.H., Kyriakou, G., Macleod, N., Tikhov, M., Lambert, R.M., 2005. J. Catal. 236 (2), 401–404.
Vlachos, D.G., 2008. Phys. Rev. E 78 (4), 046713.
Voter, A.F., 2005. Radiation Effects in Solids. Springer, NATO Publishing Unit, Dortrecht.
Wadley, H.N.G., Zhou, A.X., Johnson, R.A., Neurock, M., 2001. Prog. Mater Sci. 46 (3–4), 329–377.
K. Weissermel, H.-J. A., Industrial Organic Chemistry. Fourth ed.; WILEY-VCH: Weinheim, Germany, 2003.
Wells, D.H., Delgass, W.N., Thomson, K.T., 2004a. J. Catal. 225 (1), 69–77.
Wells, D.H., Delgass, W.N., Thomson, K.T., 2004b. J. Am. Chem. Soc. 126 (9), 2956–2962.
Wells, D.H., Joshi, A.M., Delgass, W.N., Thomson, K.T., 2006. J. Phys. Chem. B 110 (30), 14627–14639.
Xu, Y., Mavrikakis, M., 2003. J. Phys. Chem. B 107 (35), 9298–9307.
Young, W.M., Elcock, E.W., 1966. P. Phys. Soc. London 89 (565P). 735-&.
Zheng, Z., Stephens, R.M., Braatz, R.D., Alkire, R.C., Petzold, L.R., 2008. J. Comput. Phys. 227 (10), 5184–5199.